Fe–Ni-based alloys as highly active and low-cost oxygen evolution reaction catalyst in alkaline media

Lucile Magnier, Garance Cossard, Vincent Martin, Céline Pascal, Virginie Roche, Eric Sibert, Irina Shchedrina, Richard Bousquet, Valerie Parry, Marian Chatenet

Investigation of Fe and Ni-based alloys as highly-active and low-cost oxygen evolution reaction catalyst in alkaline media

Lucile Magnier [1,2], Garance Cossard [2], Vincent Martin [2], Céline Pascal [1], Virginie Roche [2], Eric Sibert [2], Irina Shchedrina [3], Richard Bousquet [4], Valérie Parry [1], Marian Chatenet [2]

[1] Univ. Grenoble Alpes, CNRS, Grenoble INP (Institute of Engineering, Univ. Grenoble Alpes), SIMAP, F-38000 Grenoble, France
[2] Univ. Grenoble Alpes, Univ. Savoie Mont Blanc, CNRS, Grenoble INP (Institute of Engineering, Univ. Grenoble Alpes), LEPMI, 38000 Grenoble, France
[3] Pierre Chevenard Research Center, APERAM Alloys Imphy, 58160, Imphy, France
[4] Product Development, APERAM Alloys Imphy, 58160, Imphy, France

Abstract

This study investigates how the chemical composition and manufacturing process of industrial Fe-Ni-alloys impact their OER performances, and unveils the nature and the activity of their active-sites. The Ni^{III}/Ni^{II} transition potential depends on the Fe-content of the Fe-Ni-alloys (Fe/Ni ratio), enabling a calibration of the surface composition. While the manufacturing process and the initial surface state of the alloys do not impact the OER performance, both the formation of a Ni-rich active-layer, whose growth depends on the presence of other alloying elements, and the surface Fe/Ni ratio drive the OER activity. Finally, regardless of the initial Fe/Ni ratio of the Fe-Ni-alloy (which varied between 0.004 and 7.4 herein), the best OER performance (beyond commercial IrO_2) was obtained for 0.2 < surface Fe/Ni ratio < 0.4. This ratio, reached upon appropriate electrochemical activation, combines numerous active-sites (high Ni^{III}/Ni^{II} capacitive response, suggesting high active area), and high efficiency (high Fe/Ni ratio).

Global warming calls for renewable electricity, which hydrogen, ideally produced *via* water electrolysis, can efficiently store [1,2]. The slow-kinetics oxygen evolution reaction (OER) that occurs in water electrolysers induces efficiency-loss in operation and high cell voltage [3,4]. Although IrO_2 is often employed as the reference OER electrocatalyst [5–7], more sustainable, active, stable and Earth-abundant catalysts must be developed: NiFe-based oxo-hydroxides ($Ni_{1-x}Fe_xOOH$) [8–15] are usable in alkaline water electrolysers [16–18], their Fe/Ni ratio determining activity, the optimum being 10-50 at.% Fe (0.11 < Fe/Ni ratio < 1) [9,13,19,20]. The active-sites' nature in $Ni_{1-x}Fe_xOOH$ remains debated [13,15]: Fe atoms [19–22], Ni atoms [9, 23–25] or a synergy between Ni and Fe sites were proposed to explain the impressive OER performances of $Ni_{1-x}Fe_xOOH$ [14,26]; for Burke *et al.*, Fe atoms in a Ni oxo-hydroxide matrix are the active-sites, the matrix providing electrical conductivity, Fe chemical stability and large active surface area support [27]. Co-precipitation, homogeneous precipitation or electrodeposition on a substrate enable to synthesize $Ni_{1-x}Fe_xOOH$ electrocatalysts of tailored crystal-size and morphology [13]. The electrocatalyst stability and lifetime depending on its adherence on the support [28–30], carbon substrate [8,31] was considered, but is not industrially viable, owing to its inherent OER instability [32,33].
Commercial stainless steels containing Fe and Ni can be activated by high-current (1770 $mA.cm^{-2}$) application in aggressive electrolyte (7.2 M NaOH at 50°C) [24], high/low potential steps in 5 M LiOH or KOH at 25°C [34,35] or *in situ* activation at 75°C under constant current (30 $mA.cm^{-2}$) in 1 M KOH [36], to form a surface layer capable of self-healing, hence enabling long-term stability [34,35] and high OER activity, as reported for stainless steels AISI 316L [34,35], AISI 304 [24], AISI 316, AISI 303 and AISI 310S [36,37].
The alloys composition (AISI 310S, AISI 316 and AISI 303, with a Fe/Ni ratio of 2.82, 6.90 and 8.26, respectively) critically influences the materials' OER activity [37], steel electrodes showing better OER activity than pure Ni and pure Fe; activated AISI 304 shows optimal performance with an ultra-thin film composed of $Ni_{0.67}Fe_{0.33}$ (Fe/Ni ratio = 0.49) [24].

Herein, the activation method developed by Moureaux *et al.* [34,35] was applied to five Fe- and Ni-based alloys with a Fe/Ni ratio ranging from 0.004 to 7.4 on wire and plate samples, to determine how alloy composition and manufacturing affect OER activity, measured at initial state, after aging and after activations. The active-layer was characterized using transmission electron microscopy coupled with X-Ray energy dispersive spectrometry (TEM-EDS), orientation and phase mapping transmission electron microscopy (TEM-ASTAR), X-ray diffraction (XRD) and X-ray photoelectron spectroscopy (XPS). The surface Fe/Ni ratio is a key parameter; its evolution during aging and activation drives the OER performance, together with an increase in Ni^{III}/Ni^{II} capacity (active-layer growth), which enables to unveil the active-sites' nature and the synergy between Fe and Ni atoms. Durability studies further demonstrate that such activated surfaces are robust for long-term OER.

RESULTS

Comparison of different grades at initial state

Five alloys, either austenitic stainless steels or Ni-based alloys were evaluated for OER. XRD evidenced different preferential grain orientations between wires (W) and plates (P) (Fig. S1). The alloy compositions in major elements (Fe, Ni, Cr, Mo, Nb) cover a range of Fe/Ni ratio between ~0 and 7.4 (Table S1).

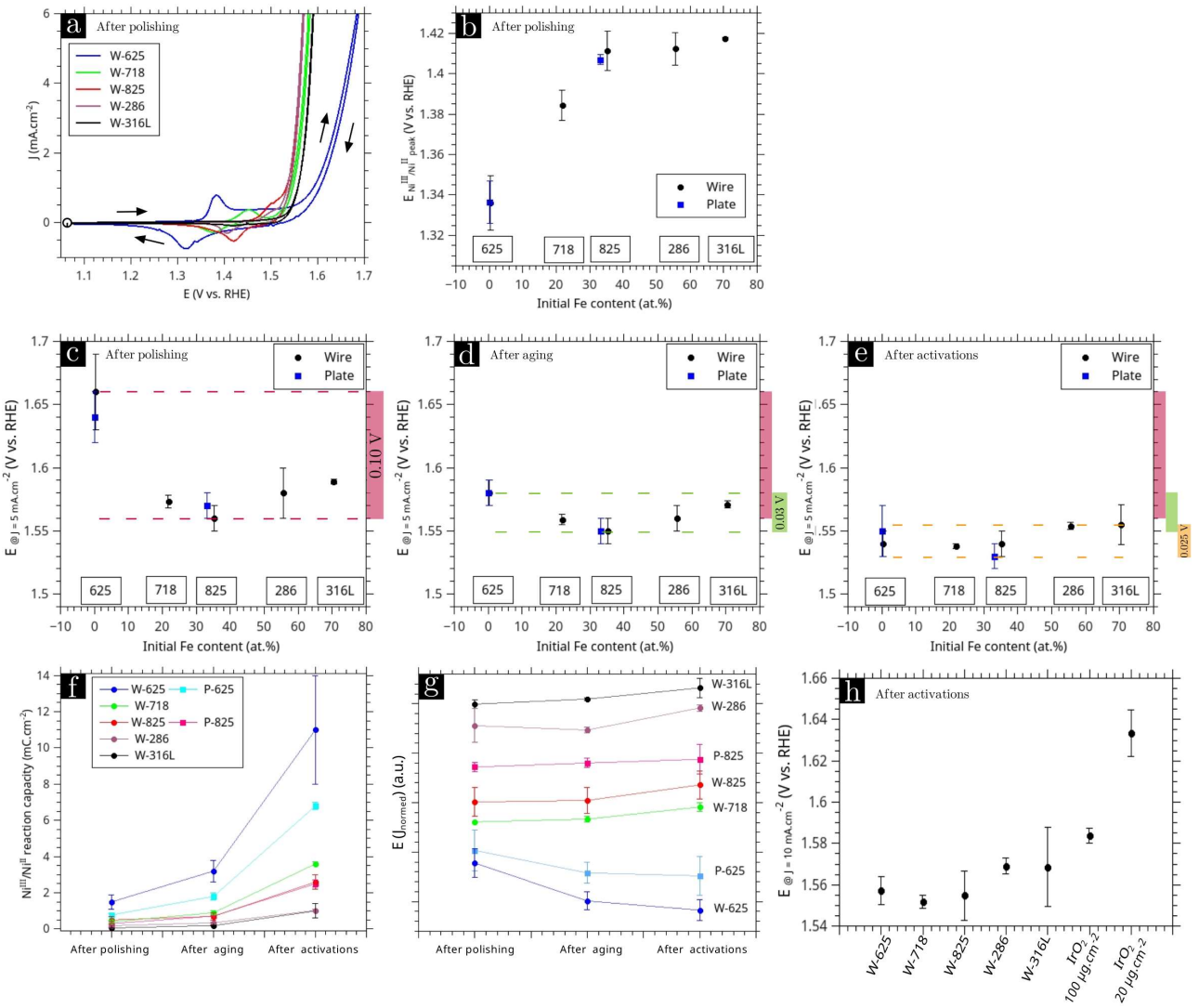

Figure 1: Electrochemical characterization of the OER performances in 0.1 M KOH at 25°C. (a) CV scans of the different alloys (wires) after polishing, performed at 50 $mV.s^{-1}$ (the start of the CVs is indicated by the dot and the scan direction by the arrows). (b) Potential of Ni^{III}/Ni^{II} reduction peak, extracted from Fig. 1a, as a function of the initial Fe-content determined by SEM-EDS (Table S1). OER potentials for wires and plates (c) after polishing, (d) after aging, (e) after activations. Potentials are measured at a current density of 5 $mA.cm^{-2}$ from Supplementary Figs. S2a to S8a. The differences between the highest and lowest potentials are plotted on the right of each graph after polishing (pink), after aging (green) and after activations (orange). (f) Evolution of the Ni^{III}/Ni^{II} reaction capacity for each grade after polishing, after aging and after activations. The value is calculated from the integration of the Ni^{III}/Ni^{II} reduction peak of the CV scans in Supplementary Figs. S2a to S8a. (g) Evolution of the Ni active-site performance: a decrease in potential corresponds to an increase in active-site performance. These values are extracted from Supplementary Figs. S2b to S8b representing the current density normalized by the Ni^{III}/Ni^{II} reaction capacity as a function of the potential. (h) OER potential at a current density of 10 $mA.cm^{-2}$. Comparison of the different grades (wires, after activations) with IrO_2 deposits on glassy-carbon electrode. The potentials for IrO_2 are extracted from the CV scans reported in Supplementary Fig. S9.

Electrochemical measurements: effects of Fe-content, manufacturing process and surface preparation

Fig. 1a reports the CV scans performed on polished wires (for plates, see Figs. S2a and S3a). Oxidation (1.35-1.5 V vs RHE) and reduction (1.3-1.45 V vs RHE) peaks attributed to the Ni^{II}/Ni^{III} transitions ($Ni(OH)_2/NiOOH$ [9,34,36,38,39]) confirm the presence of surface Ni oxo-hydroxide. Their positions depend on the alloys' Fe-content (Fig. 1b): increasing Fe-contents up to 35.3 at.% positively-shifts the Ni^{III}/Ni^{II} reduction peak [9,11,12,14,23,37]. For higher Fe-content, up to 70.5 at.%, the reduction peak potential is stable [14].

The OER slope (above 1.5 V vs RHE, Fig. 1a) reflects a variation in OER overpotential (Fig. 1c). The materials' OER performance (potential at J = 5 mA.cm^{-2}, from Figs. S2.a to S8.a) depends on the bulk Fe-content (Figs. 1c-e). For polished surfaces, Fig. 1c, the grade greatly influences performance: W-625 (1.66±0.03 V vs RHE) and W-825 (1.56±0.01 V vs RHE) exhibit the highest and lowest potential, respectively. As reported by Dionigi and Strasser's [13] for NiFe-based oxo-hydroxides [9,12,13,19,22,40], grades with 21.76 < Fe-content < 35.3 at.% yield the highest OER activity (Fig. 1c). 2.5 hour-aging at open circuit voltage (OCV) in the electrolyte (Fig. 1d) drastically decreases the OER potential of Fe-poor grades (W-625 and P-625), by 0.08 and 0.06 V respectively, and (slightly) improves the performance of other grades, hence homogenizing performance among all. Activations (alternated high/low potentials) further reduce the OER potential (Fig. 1e), the lowest potential being recorded for P-825 (1.53±0.01 V vs RHE). All grades tend towards similar OER potential after activations, insignificant variation being observed between wires and plates.

The Ni^{III}/Ni^{II} peaks coulometry (capacity, Fig. 1f) scales with the grade's initial Ni-content: W-316L, of smallest Ni-content (9.53 at.% Ni, Table S1), has the lowest initial capacity (0.06±0.01 mC.cm^{-2}); W-625 (65.6 at.% Ni) has the highest (1.5±0.4 mC.cm^{-2}). The capacity increases with aging and activations.
The Ni^{III}/Ni^{II} capacity-normalized current-density (Figs. S2.b to S8.b) reflects changes in Ni active-site performance, assuming Ni^{III} is the OER active-site [34]. The measured potential at given OER current-density ($E(J_{\text{normed}})$) decreases when the sites efficiency increases at constant active-sites number, as for W-625 and P-625 (Fig. 1g). For other grades, $E(J_{\text{normed}})$ increases or is constant, suggesting decreased or stable active-site efficiency.

After aging and activations, the alloys' catalytic performance improved; activated Fe-Ni-alloys outperform commercial IrO_2 (Figs. 1h and S9). The overpotential related to the electrochemical surface area (ECSA), which denotes the number of active sites ($\eta_{\text{-ECSA}}$ in Table 1), demonstrates the real interest of our surfaces; they outperform many materials from the literature in terms in "intrinsic OER activity". When the ECSA (Table 1) is large (high roughness), the complete surface cannot be efficiently used for OER, resulting in smaller apparent turnover frequency.

Table 1: Comparison of OER overpotential ($\eta_{\text{-geo}}$) measured in our study with reference of the literature (related to a fixed geometric current density). The electrochemical active surface area (ECSA) is also measured from the papers of the literature where appropriate CVs are given to make this estimation. The OER overpotential measured at a fixed ECSA current density ($\eta_{\text{-ECSA}}$) is also reported in this table.
[a] OER overpotential measured after activations. [b] Vertically grown FeNi LDH nanosheet arrays, *i.e.* very large developed surface. LDH = layered double hydroxide; GC = glassy carbon

Electrocatalyst	$\eta_{\text{-geo}}$ (mV, at J = 10 mA cm$^{-2}_{\text{-geo}}$)	ECSA (cm^2)	$\eta_{\text{-ECSA}}$ (mV, at J = 0.4 mA cm$^{-2}_{\text{-ECSA}}$)	Electrolyte	Reference
W-625 [a]	327 ± 7	8 ± 2	341 ± 10	0.1 M KOH	This work
W-718 [a]	320 ± 10	3.4 ± 0.1	310 ± 2	0.1 M KOH	This work
W-825 [a]	322 ± 3	2.0 ± 0.3	308 ± 12	0.1 M KOH	This work
W-286 [a]	339 ± 4	1.11 ± 0.07	304 ± 2	0.1 M KOH	This work
W-316L [a]	340 ± 20	0.9 ± 0.4	304 ± 5	0.1 M KOH	This work
IrO_2 – 20 µg.cm^{-2}	400 ± 10	-	-	0.1 M KOH	This work
IrO_2 – 100 µg.cm^{-2}	354 ± 3	-	-	0.1 M KOH	This work
FeNi LDH on FeNi foil [b]	130	1120	-	0.1 M KOH	[43]
Electrodeposited Fe-Ni film (Fe/Ni = 0.67)	280	381	265	0.1 M KOH	[9]

$Ni(OH)_2$	573	4088	-	0.1 M KOH	[44]
NiFe LDH on GC	348	94.5	300	0.1 M KOH	[44]
AISI 304 activated steels (Elox 300)	269	122	470	0.1 M KOH	[24]
3D S235 steel (phosphorization)	326	-	-	0.1M KOH	[45]
IrO_2 - 210 µg.cm^{-2}	330	-	-	0.1M KOH	[46]
316SS activated steels	254	218	190	1 M KOH	[36]
316L SS *ex situ* activated	300	-	-	1 M KOH	[35]

The Fe-Ni alloys were submitted to long-term polarization (Fig. S10.a) and highly intensive potential cycling (accelerated stress test (AST), Fig. S10.b-g): 20 000 cycles at 1 V.s^{-1} between 0.5 and 1.8 V vs RHE). Overall, the durability tests of Fig. S10 performed in 0.1 M KOH confirm previous contributions of the authors [34,35]: an activated 316L electrodes showed extensive OER durability (> 1000 h-long test) in concentrated KOH (1 M and 5 M) and concentrated (5 M) LiOH. The Fe-Ni alloys are slightly more active for dynamic operation (AST) than in stationary conditions (Fig. S10.a), in agreement with Chung *et al*. [41] and *Todoroki et al*. [42]. Moreover, they are very prone to resist harsh potential alternation (Fig. S10.b-g), that could occur during start/stop and transient operation of the alkaline water electrolyser. In all case, the OER potential reached (measured at 5 and 10 mA.cm^{-2}) is smaller than at initial state and after aging at OCV. Surfaces initially rich in Fe further activate After accelerated stress test (AST) versus After activations. Only the Fe-poor W-625 surface does not obey this trend (even though its activity post AST remains high); this agrees with Todoroki et al., who showed that pure Ni surfaces do not improve after such harsh AST, on the contrary to Fe-rich alloys of the Austenitic stainless-steel family) [47].
This high stability of the obtained Fe-doped Ni oxo-hydroxide layer likely originates from the way it forms, by dissolution/redeposition of the alloy's base components: an active layer adheres stronger on its substrate when formed by exsolution, as demonstrated by Neagu *et al*. [48], which confers self-healing properties to the prepared electrodes. The polishing states (metal/electrolyte interface roughness) only slightly modifies the OER activity/durability (Figs. S11.a,b).

The faradaic efficiency towards OER was evaluated for the Fe-Ni alloys. Two complementary techniques were used, the rotating ring-disk electrode (RRDE) to directly measure the evolved O_2 and inductively-coupled plasma mass-spectrometry (ICP-MS) analyses, to dose potential metal dissolution in the electrolyte. From the results presented in Figs. S12-S13 (RRDE) and Table S2 (ICP-MS), consequent metal dissolution from the alloys can be ruled out. This means that, whatever the Fe-Ni alloy considered, the oxidation current measured upon OER CVs near-fully originates from oxygen evolution, once the active layer is formed on the alloy surface.

(Micro)structural characterisation of the active-surface-layer

The active-surface-layer developed at the alloy/electrolyte interface after polishing, aging and activations is presented in Figs. 2a-d. W-316L, of lowest Ni-content, has the thinnest active-surface-layer: 9.4±2.0 nm (Fig. 2a). This agrees with the weak Ni^{III}/Ni^{II} capacity increase after aging and activations (Fig. 1f, 1.0±0.4 mC·cm^{-2} after activations), reflecting the low amount of Ni active-sites. W-825 (Fig. 2b) and W-718 (Fig. 2c) have active-surface-layers of 20.3±5.4 and 34.3±6.3 nm, respectively, in line with their larger Ni^{III}/Ni^{II} capacity (2.6±0.4 and 3.6±0.1 mC.cm^{-2}). W-825 and W-718, have variable active-surface-layer thickness, with maximal

deviation from the average of 15.1 nm and 17.7 nm, respectively. W-625 has thicker active-surface-layer (38.8±2.7 nm, Fig. 2d), which coincides with its large capacity 11±3 mC.cm^{-2}.

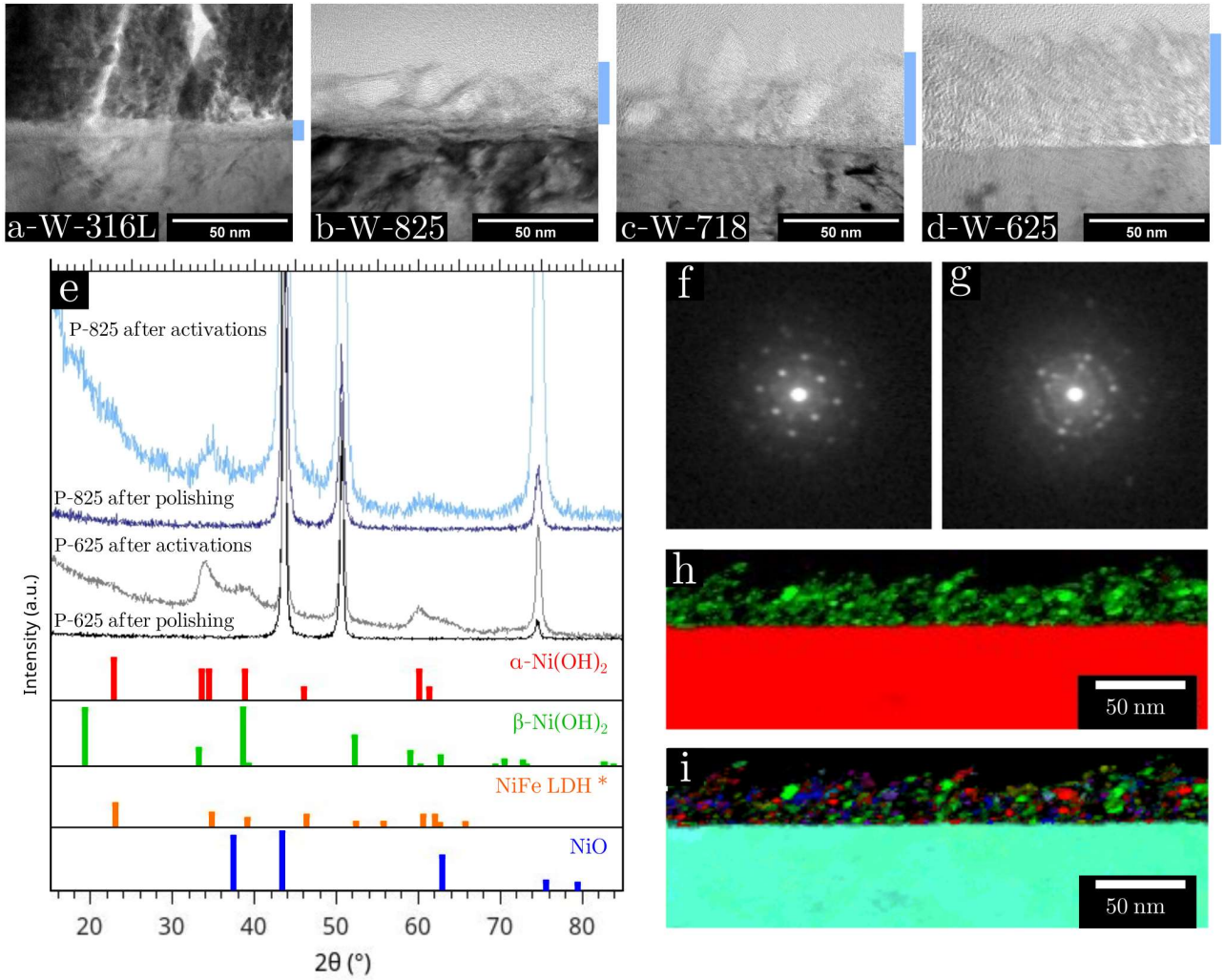

Figure 2: TEM images of the samples after four activations (a) W-316L, (b) W-825, (c) W-718 and (d) W-625. The active-surface-layer is outlined by the blue area on the right side of each image. For the TEM sample preparation using FIB-SEM, a protective layer was deposited over the oxide-layer: platinum for W-316L and carbon for W-825, W-718 and W-625. (e) Grazing incidence X-ray diffraction (GI-XRD) analysis of P-625 and P-825 after polishing and after activations. The reference patterns for α-Ni(OH)$_2$ (red, rhombohedral, ICDD no. 00-038-0715), β-Ni(OH)$_2$ (green, hexagonal, ICDD no. 00-057-0907), NiFe LDH (orange, rhombohedral, ICDD no. 00-35-0965*) and NiO (blue, cubic, ICDD no 00-004-0835) are displayed. Diffraction pattern of pixel in the active-surface-layer highlighting: (f) a well-crystallized structure and (g) a nanocrystallized structure. (h) ASTAR phase mapping generated by comparing the diffraction patterns to the austenitic phase (in red, identified using GI-XRD) and to the NiO cubic structure (in green, matching the active-surface-layer structure, see Figs. 2f and S14). (i) ASTAR crystallographic orientation mapping [49], using the same phases as Fig. 2h, highlighting the nanocrystallized structure of the active-surface-layer with no preferential orientation. Both Figs. 2h and 2i include the uncertainty related to the indexation quality (black pixels are those that do not match well with the proposed phases).
*ICDD no. 00-35-0965 corresponds to FeNi LDH structure according to Dionigi *et al.* [50]

Both P-625 and P-825 have a fcc bulk structure (grazing incidence X-ray diffraction (GI-XRD) after polishing, Fig. 2e). Additional small/wide peaks appear with the active-surface-layer formation, (GI-XRD after activations, Fig. 2e) the bulk fcc peaks remaining (thin oxide-layer). Comparison with theoretical α-Ni(OH)$_2$, β-Ni(OH)$_2$, NiFe LDH and NiO peaks, identifies the active-surface-layer to α-Ni(OH)$_2$ or NiFe LDH. The relatively broad peaks' width related to nanocrystallized structure does not allow an exact identification of the layer structure.

According to the TEM analyses, the active-surface-layer is porous and nanocrystallized: multitude of spots distributed on circles in the diffraction patten in Fig 2.g, and grains below 5 nm in Fig 2.i (with no preferential orientation).The active-surface-layer TEM diffraction pattern in Fig. 2f highlights a cubic structure that matches cubic NiO, as plotted in Fig. S14. Phase mapping (Fig. 2h) highlights a bulk austenitic phase (red) and a NiO cubic active-surface-layer (green). The conversion of α-$Ni(OH)_2$ or NiFe LDH (detected using GI-XRD) into NiO (detected using TEM) may come from the TEM samples focused ion beam (FIB) preparation.

Active-surface-layer composition

According to TEM-EDS elemental profiles (Fig. 3), though Fe remains the main component in the active-surface-layer of W-316L (Fe/Ni ratio > 1 after activations), the Fe-content decreases, the Ni-content is rather stable and Cr-content approaches zero. W-825 and W-718, initially containing more bulk Ni than Fe, show decreased Fe-content, Cr disappearance from the layer (as for W-316L), their Fe/Ni ratio remaining below 1 after activations. W-625, whose major element is Ni, shows a markedly-increased Fe-content in the active-surface-layer. Except for W-316L, the grades reach active-surface-layer compositions of 5-10 at.% Fe and 15-20 at.% Ni, evidencing that the active-surface-layer composition homogenizes for all samples after activations.

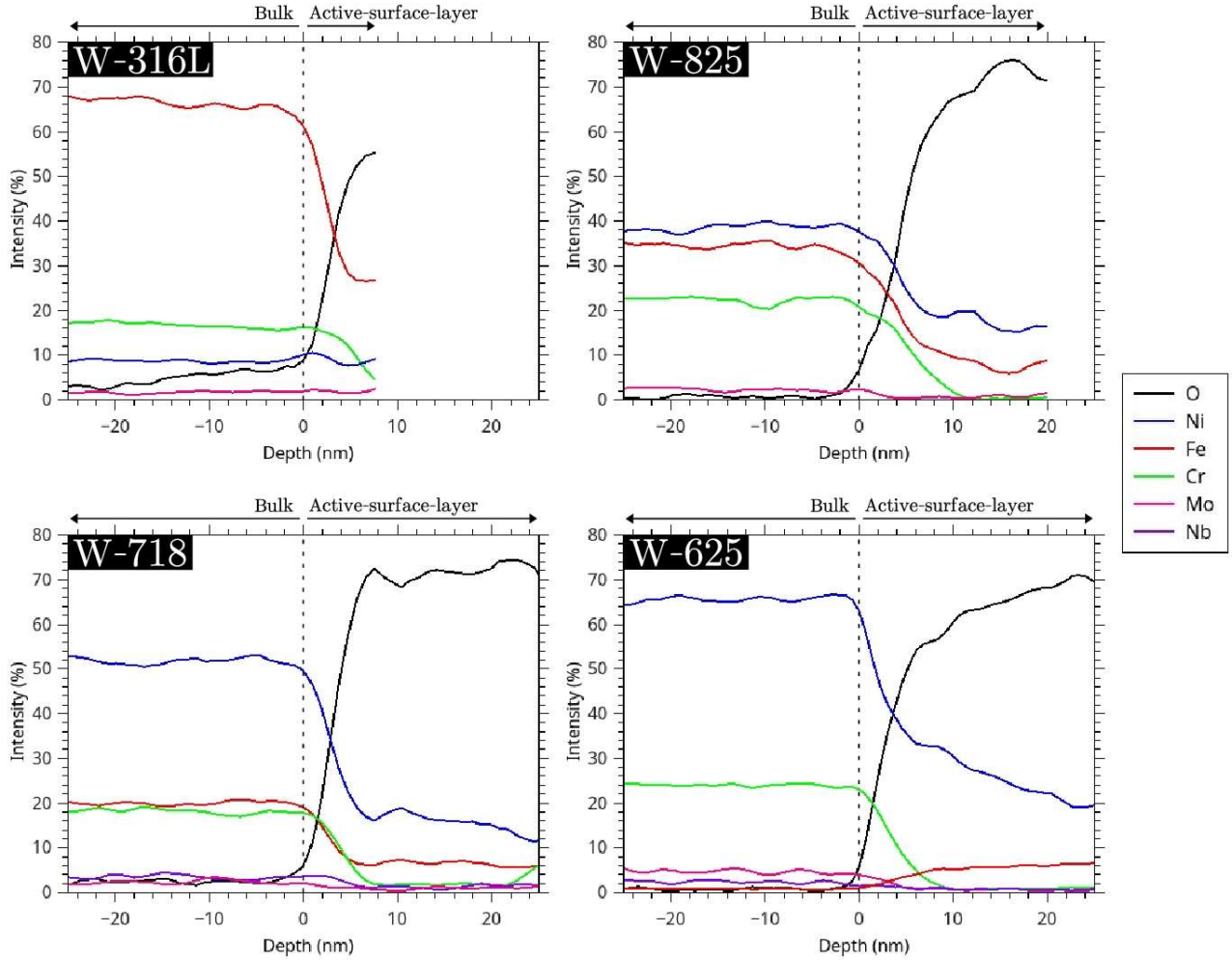

Figure 3: TEM-EDS analysis: chemical composition profiles performed on samples after activations. The negative depths correspond to the bulk and the positive depths to the active-surface-layer. Only the major elements are plotted on these graphs.

Figure 4 displays Ni 2p, Fe 2p and Cr 2p photoelectron lines of W-718 and W-625; Mo 3d and Nb 3d peaks are reported in Fig. S15. As satellites structures are present and since $Ni(OH)_2$ and

NiOOH binding energies are too close to be separated, the Ni 2p3/2 signal was deconvoluted by three main peaks, at 852.6, 853.7 and 855.8 eV, attributed to Ni^0, NiO and Ni^{2+}/Ni^{3+}, respectively [37,51,52]; Fe 2p3/2 peaks at 706.7, 710.7 and 712.7 eV were assigned to Fe^0, Fe_2O_3 and FeOOH, respectively [53,54]; for Cr 2p3/2, the 573.6, 575.9 and 577.2 eV peaks correspond to Cr^0, Cr_2O_3 and $Cr(OH)_3$, respectively [52,54].

On as-received polished W-718, Figs. 4a-c, XPS detects a metallic layer and a native-oxide-layer containing both Ni, Fe, Cr, Mo and Nb (around 10 nm depth). After aging, the metallic peak decreases, reflecting oxide-surface-layer growth. The Ni oxo-hydroxide peak significantly increases, suggesting that a Ni-rich layer develops. After activations, the oxide-layer grows, the metallic peaks disappear and the intensity of the Cr, Mo and Nb peaks sharply drop (Figs. 4c and S15). Similar observations were made on W-825, P-825 and W-316L.

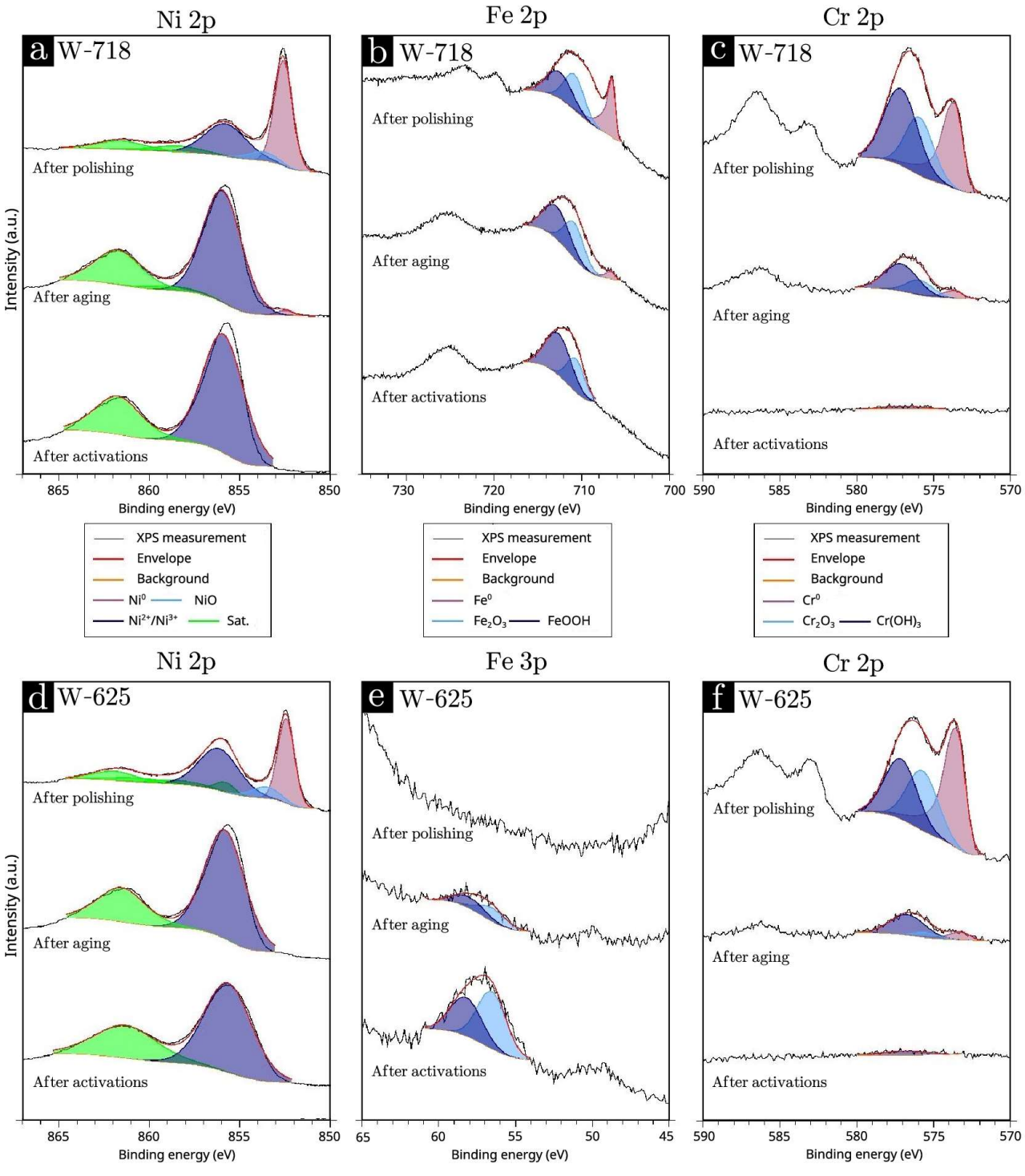

Figure 4: XPS analysis of W-718: (a) Ni 2p, (b) Fe 2p and (c) Cr 2p. XPS analysis of W-625: (d) Ni 2p, (e) Fe 3p and (f) Cr 2p. The fitting parameters used are reported in Tables S3 to S5. Three samples per grade were analysed by XPS after polishing, aging and activations.

W-625 and P-625 behave differently: the Fe 3p line is considered in XPS (Fig. 4e), because the Fe 2p peaks overlap with a Ni LMM Auger one. The correspondence of the Fe 2p and Fe 3p fits was validated by analysing these peaks for other grades, with lower Ni-content. The Fe 3p peak contains two contributions at 55.4 and 56.8 eV, corresponding to Fe_2O_3 and FeOOH [53,54]. The Ni 2p and Cr 2p peaks exhibit a similar trend as the other grades with aging and activations: a Ni-rich oxo-hydroxide-layer grows (the metallic peaks disappear and the Cr peak decreases). The Fe 3p peak analysis, Fig. 4e, highlights the initial absence of Fe in this grade. After aging and activations, Fe-oxide is detected, confirming the TEM-EDS measurement: Fe incorporates during aging (without current or potential application) and increases upon activations.

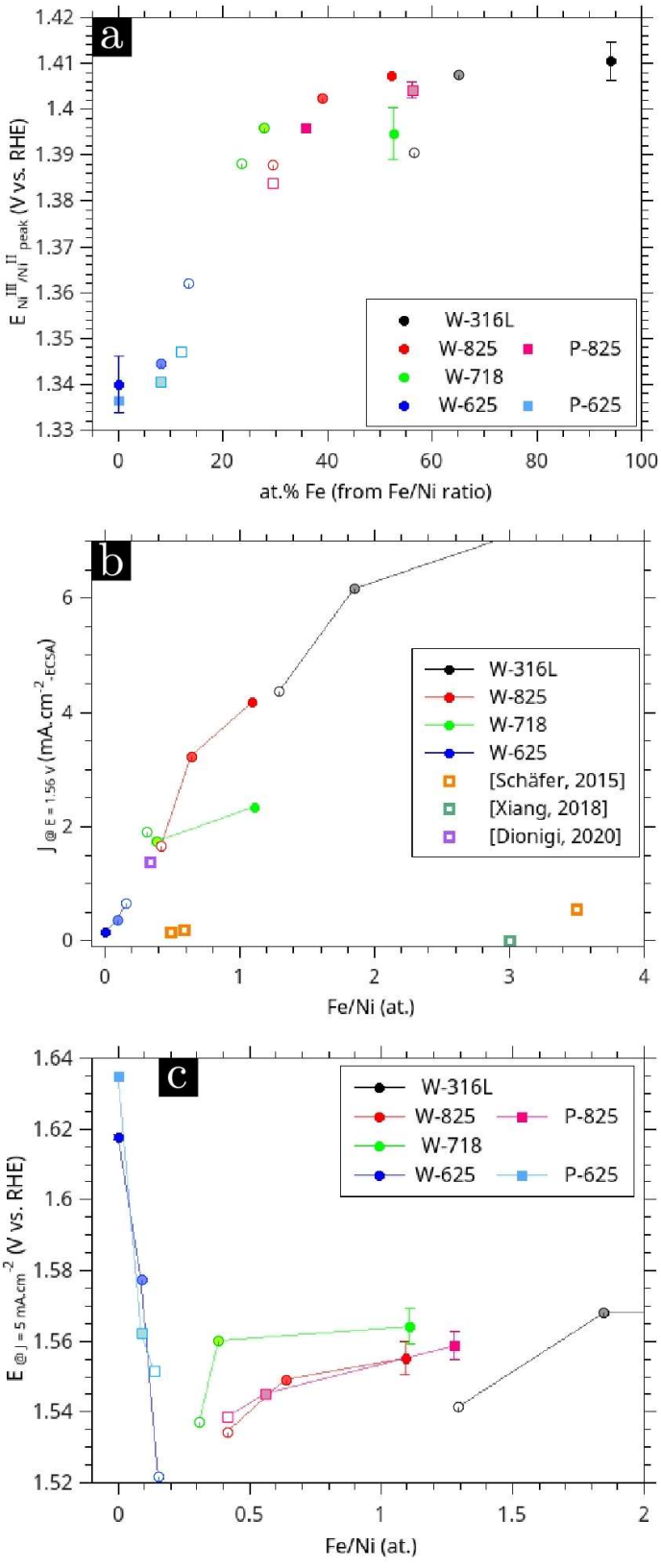

Figure 5: (a) Potential of Ni^{III}/Ni^{II} reduction peaks as a function of the Fe content (at.%) determined from the Fe/Ni ratio measured by XPS. To calculate the Fe atomic percentage, an alloy containing only Fe and Ni is considered.
(b) Ni active-site activity as a function of the Fe/Ni ratio in the surface layer. For each point, the geometric current density ($mA.cm^{-2}_{-geo}$) is taken for a potential of 1.56 V vs RHE, corresponding to the OER region. This value is then normalized by the ECSA value to be expressed in $mA.cm^{-2}_{-ECSA}$. The ECSA value for W-316L in the initial state being very low, the error on the measurement is large; the corresponding Fe/Ni ratio of 16.0 is therefore not reported on the graph.
[Schäfer, 2015] reports AISI 304 activated steels with different Fe/Ni ratios: 0.49 (Elox300), 0.58 (Elox480) and 3.5 (EloxCycl) [24]. These data support the trend of an increase in Ni active-site activity with higher Fe/Ni ratio. [Xiang, 2018] corresponds to a vertically grown FeNi LDH nanosheet arrays on FeNi foil, *i.e.* very large developed surface [43]. The reported Fe/Ni ratio is the one of the interfacial hydroxide (Fe/Ni = 3). [Dionigi, 2020] refers to a NiFe LDH on GC with a Fe/Ni ratio of 0.33 [44]. The Dionigi reference presents a similar behaviour as our NiFe alloys. The low J ($mA.cm^{-2}_{-ECSA}$) values for Schäfer's and Xiang's references can be explained by the large ECSA of the samples, *i.e.* a low current density per Ni site.
(c) Correlation of OER performance with the oxide-layer chemical composition: OER potential (at 5 $mA.cm^{-2}$) as a function of the Fe/Ni ratio measured by XPS.
The initial state is represented by the solid dots (●); after aging corresponds to the lighter dots (●) and after activations is reported with the open circles (○).

DISCUSSION

The Ni^{III}/Ni^{II} reduction peak potential strongly depends on the bulk materials Fe-content (Fig. 1b). Furthermore, the Ni^{III}/Ni^{II} peak positively-shifts for increased Fe-content (Fig. 5a), which originates from atomic-scale structure/organization. Assuming that GI-XRD (Fig. 2e) identified the α-$Ni(OH)_2$ phase (or a NiFe LDH phase) in the active-surface-layer after activations, as on Fe-doped $Ni(OH)_2$[23], mixed Ni-Fe oxo-hydroxides [14] and activated steels [34], Fe is likely

substituted to Ni in this α-$Ni(OH)_2$ matrix [19,55]; this possibly induces a different electronic environment of Ni in the α-$Ni(OH)_2$ phase [21] and a symmetry-distortion around Ni with increasing Fe-content [56]. Beyond 40 at.% Fe, the Ni^{III}/Ni^{II} potential stabilizes around 1.4 V vs RHE: the limited solubility of Fe^{3+} in α-$Ni(OH)_2$ may yield a Fe-rich phase (FeO_xH_y) for higher Fe-content, that coexists with the previous Fe-containing α-$Ni(OH)_2$ phase [19,20]. Figure 5a is therefore a master-curve to determine, from the CV scans, the Fe-content in NiFe oxo-hydroxides.

Crystallographic orientations of the OER active phase is believed to influence the OER activity [57,58,23]. Herein, wires and plates have different preferential crystallographic orientations (XRD, Fig. S1); OER performances (Figs. 1c-e) slightly vary between wire and plates for the 625 and 825 grades, denoting a poor bulk crystallographic orientation effect on OER performance. Indeed, no epitaxial growth of the active-surface-layer was induced since this layer is nanocrystallized with no preferential crystallographic orientations (see Fig. 2i). The metals surface preparation also has no impact on OER (Fig. S11), demonstrating that the active-surface-layer formation mostly determines the OER activity; these grades can be highly-active for OER without any surface preparation step.
Hence, chemical composition is the main parameter influencing OER performance (Fig. 1c) with an optimum for 10 < at.% Fe < 50 in $Ni(OH)_2$/NiOOH [13]. Grades with lower Fe-content exhibit high OER potential, owing to the poor catalytic activity of pure $Ni(OH)_2$ [12,20]. Fe-rich grades (above 50 at.%) exhibit intermediate performance, because an inactive FeO_xH_y phase forms, overall decreasing the apparent OER activity [19,20]. Despite the addition-elements present in the grades (mainly Cr and Mo), the samples follow the trend described for NiFe-based oxo-hydroxide catalysts: the Fe- and Ni-content (Fe/Ni ratio) remains the main criterion determining OER performances.

W-625 and P-625 have a very low initial Fe-content (Fig. 4e); however, Fe was detected in the active-surface-layer after aging and activations (Figs. 3 and 4e). The positive-potential-shift of the Ni^{III}/Ni^{II} reduction peak (Figs. S2 and S4) confirms this Fe-enrichment (Figs. 1b and 5a). This Fe-content increase correlates with the strongly-improved OER performance (Figs. 1c-e): for W-625 and P-625, the OER potential is drastically reduced after aging and activations. Fe-incorporation into Ni-based electrocatalysts is known to significantly accelerate OER [11,12,20,22,23,27,40]. Fe-incorporation into NiOOH enhances conductivity, while partial charge-transfer between Fe and $Ni^{3+/4+}$ promotes OER kinetics [11], in line with the improved performance of Ni active-sites with aging and activations of W-625 and P-625 (Fig. 1g). Fe-incorporation increases the Fe/Ni ratio and leads to a more favourable range of Fe-content of the surface composition.
Table S8 and Figures S16-S17, relative to a 99.999% pure Ni (W-Ni), for which surface-enrichment by migration of Fe contained in the bulk is impossible, show that Fe impurities in the electrolyte (prepared from KOH pellets, 85%) are mostly responsible for Fe-incorporation in the oxide-layer [11,12,20].

TEM-EDS (Fig. 3) and XPS analyses (Figs. 4 and S15) demonstrate that the OER active-surface-layer predominantly contains Ni and Fe. The initially relatively-high Cr content (Table S1) drastically reduces from the surface layer after aging and activations. Based on different grades of narrower compositions (67-72 at% Fe, 7-21 at% Ni, 1-8 at% Cr), Todoroki *et al.* explained such trend [36,37] by solubility differences in alkaline media: Ni-oxides are stabilized, unlike Fe- and Cr-oxides [24,59]. The Ni^{III}/Ni^{II} capacity plot (Fig. 1f) demonstrates the growth of a Ni-rich oxo-hydroxide-layer upon aging and activations, yielding more Ni surface-sites. Correlation with the layer thickness (TEM analysis, Fig. 2) indicates that Ni-rich bulk alloys exhibit larger Ni^{III}/Ni^{II} capacity increase with aging and activations, and thicker oxide-layer.

W-Invar (65.4 at.% Fe, 34.1 at.% Ni, Tables S9, S10, Figs. S18 and S19),whose Fe/Ni ratio (1.92) is comparable to W-825 (0.97) and W-286 (2.44), exhibits stable OER potential (at 5 $mA.cm^{-2}$) with aging and activations (Fig. S19.a), higher than for W-825 and W-286. Neither grade show Ni active-site performances improvement (Figs. S19.d and 1g). The Ni^{III}/Ni^{II} capacity of W-Invar remains very low even after activations (0.5±0.1 $mC.cm^{-2}$, Fig. S19.b), well below the smallest value of the tested steels (W-316L: 1.0±0.4 $mC.cm^{-2}$). Thus, minor alloying elements (mainly Cr and Mo) have an important role in the Ni-rich active-layer creation for Fe-rich grades. Studying pure Ni (99.999%) revealed that the OER performance could be improved solely by Fe-incorporation (without the presence of additional elements), suggesting that the active-layer formation may depend on the bulk Fe-content: for Fe-poor grades, Fe-incorporation increases the OER performance with the development of a thick Ni-oxide layer; for Fe-rich grades, a Ni-rich layer grows with a decrease in addition-element content in the surface layer (Cr, Mo, Nb, etc., Figs. 4 and S15), which are therefore essential in the layer's formation and growth.

After activations, each active-surface-layer mainly contains Fe and Ni (TEM-EDS and XPS). Plotting the activity of the Ni active-sites versus the Fe/Ni ratio in the layer (Fig. 5b) shows that higher Fe/Ni ratio yield better active-sites' performance: better OER performance per number of Ni sites are obtained for as-high-as-possible Fe-content in the active-layer. In comparison with NiFe-LDH or other activated steels, our NiFe alloys have a similar or better Ni active-sites activity for the same Fe/Ni ratio.

The number of Ni active-sites is also crucial in the catalyst's OER performance. Although W-316L has the highest initial Fe-content, its OER activity after activations is poor (Figs. 1e,h), owing to a very small increase in Ni^{III}/Ni^{II} capacity (Fig. 1f) and a very small oxide-layer thickness (Fig. 2a). Its composition (70.5 at.% Fe, 9.53 at.% Ni) cannot develop a Ni-rich active-layer with the present activation method, in agreement with Todoroki *et al.* [37]: the Fe/Ni ratio and the capacity to generate a catalyst layer (with a large surface area) are the dominant criteria to obtain the best OER performances.

Fig. 5c correlates the OER potential with the layer's chemical composition. The very high initial Fe/Ni ratio (around 16.0) of W-316L significantly decreased to 1.8 and 1.3 after aging and activations, lowering the OER potential: 1.577, 1.568 and 1.541 V vs RHE, initially, after aging and after activations.
W-825, P-825 and W-718, with an initial Fe/Ni ratio of 1.1, 1.3 and 1.1 respectively, exhibit lower OER potentials: 1.555, 1.559 and 1.564 V vs RHE. Aging reduces both the Fe/Ni ratio (0.6, 0.6 and 0.4) and OER potential (1.550, 1.545 and 1.560 V vs RHE), activations decreasing them even more: Fe/Ni ratio of 0.4, 0.4 and 0.3, and OER potential of 1.534, 1.539 and 1.537 V vs RHE, respectively. This evolution of Fe/Ni ratio follows the layer's Ni-enrichment (XPS, Fig. 4) following Ni-oxides' stabilization, unlike Fe- or Cr-oxides [24,59]. For these grades, the OER performance increase is therefore correlated to the decreased Fe/Ni ratio, which converges to 0.3-0.4.
The Fe/Ni ratio of W-625 and P-625 initially tends to zero. Aging induces Fe-incorporation into the oxide-layer (from electrolyte impurities), leading to a ratio of 0.09 for both samples, and OER potentials decreased to 1.577 and 1.562 V vs RHE, respectively. Activations further increase the Fe/Ni ratio (0.2 and 0.1) and decrease the OER potential (1.522 and 1.552 V vs RHE). For grades with very low initial Fe-content, increased Fe/Ni ratio improves OER.
The wide range of chemical composition of the alloys tested (bulk Fe/Ni ratio between 7.40 and 0.004 (Table S1) and between 16 and 0 in the native oxide-layer (XPS)) enables to correlate the OER activity increase to an optimized Fe/Ni ratio, which tends towards 0.2-0.4. Schäfer *et al.* also reported optimized performance for steels composed of 67% Ni and 33.0% Fe (Fe/Ni ratio of 0.49) [24], the optimum being 25% Fe (Fe/Ni ratio of 0.33) for mixed Ni-Fe catalysts [19].

CONCLUSION

Fe- and Ni-based alloys of different chemical compositions and different crystallographic orientations between wires and plates were studied as alkaline OER electrocatalysts. Their bulk chemical compositions strongly influence their initial electrochemical performances, unlike the manufacturing and surface preparation processes.
Grades containing 21.8-35.3 at.% Fe are initially optimal for fast OER, as reported for NiFe oxo-hydroxides catalysts. Aging (2.5 hours in 0.1 M KOH) and activations (alternated high/low potentials) further reduce the OER overpotential by thickening the Fe-doped Ni oxo-hydroxides layer.
This layer's Ni^{III}/Ni^{II} capacity and Fe/Ni ratio determine the apparent OER kinetics: the Fe-Ni-alloys must develop a thick Ni-rich active-surface-layer (large number of Ni active-sites) and efficient Ni active-sites (large Fe/Ni ratio). Efficient active-sites and high Ni^{III}/Ni^{II} capacity is optimal for $0.2 < Fe/Ni < 0.4$.
Reaching this ratio is possible for a very wide range of initial alloy composition ($0.004 <$ initial $Fe/Ni < 7.4$): Fe-poor grades are optimized by Fe-incorporation (impurity contained in the electrolyte), while Fe-rich grades show Ni-enriched oxide-layer (selective dissolution of Fe, Cr, etc.), these alloying elements favouring the development of the Ni-rich active-layer. Both processes are emphasized by potential cycling.
As a result, whatever the Fe and Ni contents of the initial alloy, one can easily obtain remarkable OER activity (outperforming commercial IrO_2) and reasonable durability upon alternated potential application (which proceeds upon water electrolyser coupling to renewable sources of electricity), though alloys with low initial Fe content (e.g. 625) seem less robust to harsh potential alternation than Fe-richer ones.

Acknowledgments
This work was funded by Carnot EF (NICKEL project); VP, VR, MC and ES, thank Pierre Joncourt and William Ait Idir, who participated to a preliminary study that ended up on this project.
The research has benefited from the characterization equipment of the Grenoble INP – CMTC platform supported by the Centre of Excellence of Multifunctional Architectured Materials ''CEMAM'' (grant ANR-10-LABX-44-01) funded by the ''Investments for the Future'' Program. All authors thank Grégory Berthomé for the XPS measurements, Gilles Renou for the TEM analysis, Stéphane Coindeau and Thierry Encinas for XRD measurements. The internship of GC was funded by the DAEMONHYC project, supported by the "France 2030" government investment plan managed by the French National Research Agency, under the reference "ANR-22-PEHY-0010".

Author contributions
C.P., V.R., E.S., M.C. and V.P. designed the project study. I.S. and R.B. provided the samples. L.M. carried out the experiments and analysed the data, except for the following; G.C. and M.C. performed the rotating ring-disk experiments and evaluated the corresponding OER faradaic efficiency; G.C. made the accelerated stress tests; V.M. made the ICP-MS measurements to evaluate the extent of metal dissolution upon OER. C.P., V.R., E.S., M.C., V.P., I.S and R.B. helped discussing the results. All authors contributed to the preparation of the manuscript.

Competing interests
The authors declare no competing interests.

Additional information

Supplementary information

METHODS

Materials. Five Fe- and Ni-based alloys were studied: APERAM 316L, IMPHY 286, IMPHY 825, IMPHY 718 and IMPHY 625. These grades, manufactured by Aperam company as wires with diameters between 5.00 and 5.94 mm, were then cut into cylinders of 5 mm height (see Fig. S20a). For IMPHY 825 and IMPHY 625, 2 and 2.2 mm thick (respectively) plates were also analyzed by cutting 15 mm diameter discs. The set of grades studied, the label used in this article and the processing method are reported in Table 2.

Table 2: Details of the main characteristics of the different grades supplied by Aperam company. The column "Fe-Ni alloy" is the commercial name of the alloy and the column "Label" is the name that is used in this article to refer simply to the samples. The "Process" column gives the indication of the processing of the sample. The "Geometric surface" column is the active area tested electrochemically (used to calculate the current density).

Fe-Ni alloy	Label	Process	Geometric surface (cm^2)
APERAM 316L	W-316L	Wire	0.246
IMPHY 286	W-286	Wire	0.277
IMPHY 825	W-825	Wire	0.196
IMPHY 825	**P-825**	**Plate**	1.327
IMPHY 718	W-718	Wire	0.246
IMPHY 625	W-625	Wire	0.196
IMPHY 625	**P-625**	**Plate**	1.327

Surface preparation. The analyzed surfaces underwent several grinding steps starting with SiC abrasive discs (P320, P600, P1200, P2400) followed by polishing with diamond suspension (3 µm and 1 µm). A final mechanical-chemical polishing step was performed with a colloidal silica solution (OPU NonDry, 0.04 µm, Struers). Cleaning and rinsing were performed with ethanol and ultra-pure water (18.2 MΩ.cm, < 3 ppb total organic carbon, Milli-Q system, Millipore, Merck). The polished samples were placed in PTFE tubes (wires) or Origalys sample holder (plates) to be fixed on a rotating electrode during electrochemical tests (see Fig. S20b).

Preparation of IrO_2 samples. IrO_2 inks were prepared from IrO_2 powder (Iridium (IV) oxide, Premion, 99.99% (metal basis), Ir 84.5% min, Alfa Aesar), 5 wt.% Nafion® dispersion (1100EW, Sigma Aldrich), isopropyl alcohol (IPA, HPLC grade Fisher Chemical)) and ultra-pure water. Two inks were prepared with different loadings: 20 $\mu g \cdot cm^{-2}$ (ink A) and 100 $\mu g \cdot cm^{-2}$ (ink B). A mass of 2.0 mg (10 mg) of IrO_2 powder was weighed into a pillbox, for ink A (respectively for ink B). Volumes of 3.40 mL (3.39 mL) of ultrapure water, then 1.70mL (1.70mL) of IPA and finally 2.3 µL (11.32 µL) of Nafion® dispersion were added to the pillbox. A content of 5 wt.% Nafion® / 95 wt.% IrO_2 was weighed, and a ratio of 1/3 IPA - 2/3 H_2O was kept. The synthesized ink was placed in an ultrasonic (US) bath for homogenization. A carbon electrode was polished to 1 µm, cleaned successively 5 min with US in acetone, ethanol and ultrapure water and then placed in an oven at 90°C for 20 min. A volume of 10 µL of synthesized ink was deposited on the surface of the carbon electrode (0.196 cm^2) and dried until evaporation of the solvents.

Electrochemical set up. Electrochemical measurements were performed in a three-electrode glass cell under Argon flow at room temperature (25°C). The electrolyte, KOH at 0.1 M, was

prepared with KOH pellets (85%, Alfa Aesar) and ultra-pure water. The sample is fixed to a rotating electrode (1600 rpm imposed during the measurement) and used as working electrode. Pt was used as counter electrode and [Hg/HgO – 0.1 M KOH] was used as reference electrode (+ 0.926 V vs RHE). In this work, all potentials are expressed versus the RHE. A numerical potentiostat-galvanostat (VMP3, Bio-Logic®) was used to perform the electrochemical measurements.

OER performance determination. Cyclic Voltammetries (CV) were performed between 1.061 and 1.761 V vs. RHE at a scan rate of 50 $mV.s^{-1}$ (minimal impact of the scan rate on the measured potential is demonstrated onFig. S21). For each result presented in this article, ohmic drop was corrected, based on impedance spectroscopy measurement. The current densities are referred to the "geometric surface" value, reported in Table 2. For each result presented, three repetitions were performed to estimate the measurement error. Eleven CV scans were successively performed for the characterization of one state, and the 11^{th} CV is used to characterize the stable state of the material. The potential required to reach a given current density is the parameter indicating the reaction kinetics. The OER performances of the different samples are thus given by comparing the potentials at a current density of 5 $mA.cm^{-2}$ or 10 $mA.cm^{-2}$. For commercial IrO_2 samples, two loading were investigated, 20 $\mu g.cm^{-2}$ and 100 $\mu g.cm^{-2}$, leading to OER potentials at 10 $mA.cm^{-2}$ of 1.63±0.01 V and 1.584±0.03 V, respectively.

Characterization of the initial state. The initial state performance characterization was performed by recording a first CV scan just after the sample was immersed in the electrolyte. For the comparison with IrO_2, the deposits on the carbon electrode were characterized by a CV scan performed after immersion of the electrode in the electrolyte.

Impact of aging in 0.1 M KOH. After the initial state, the samples were placed at open circuit voltage (OCV) for 2.5 hours. A new succession of eleven CV scans was then performed to determine the impact of aging in the electrolyte (the 11^{th} CV is also used to characterized the stable state).

Impact of activations. After the aging period, the samples underwent the activation protocol proposed by Moureaux *et al.*[35]. The first part of this protocol (step 1) is a polarization at E = 1.581 V vs. RHE during 10 min, then at E = 0.981 V vs. RHE during 5 min. The second stage (step 2) consists of two CV scans performed between 1.061 and 1.581 V vs. RHE, at a scan rate of 5 $mV.s^{-1}$. Steps 1 and 2 are repeated 12 times. To maximize the performances, this activation protocol was repeated four times on each sample, and is subsequently referred to as the "impact of activations".

Durability assessment using an accelerated stress test (AST). The robustness of the Fe-Ni alloys against harsh potential variations (that can occur upon start/stops of real alkaline water electrolyser cells) was tested by applying the AST protocol suggested by Todoroki *et al.* [47]and Fujita *et al.* [60]. The AST consists of repeated triangle-wave potential cycles between 0.5 and 1.8 V vs RHE at 1 $V.s^{-1}$ for 20 000 cycles. In the present case, the OER performance was measured after polishing (or after activations), and then after 100, 500, 1000, 5000, 10000 and 20000 cycles of AST, through a CV recorded at 20 $mV.s^{-1}$ in 0.1 M KOH at 25°C between 0.5 and 1.65 V vs RHE.

Faradaic efficiency assessment by rotating ring-disk electrode measurements. A change-disk rotating ring-disk electrode tip with a platinum ring from PINE instruments (model E6R1Pt) was mounted on a PINE MSR rotator. The disk consisted of either a cylinder of

polycrystalline Pt electrode (from PINE) or of home-made Fe-Ni alloy from the studied series, machined at the proper dimensions and carefully mirror-polished before use.
The important steps of this procedure are as follows.

1 - All the measurements were performed at 1500 rpm. In these conditions, for the electrolyte employed (0.1 M KOH at 25°C), assuming the values of O_2 diffusion coefficient ($1.6\ 10^{-5}$ $cm^2\ s^{-1}$), solution kinematic viscosity (0.01 $cm^2\ s^{-1}$) and the dimensions of the RRDE tip (disk radius = 0.25 cm, ring inner radius = 0.325 cm), the theoretical transit time (see [61,62] for details) for O_2 is ca. 0.55 s. The experimental times at which the disk and ring maximum currents were measured upon the OER voltammetries was superior to this value (ca. 1 s), and this can originate from the hindrance of O_2 bubbles in the KOH electrolyte that are transported from the disk outer radius to the ring inner radius. For this reason, the ring current time was corrected by ca. 1 s for all the experiments presented hereafter.

2 - The collection efficiency (N) of the rotating ring-disk electrode, in theory 25% for this RRDE tip, was measured for the hydrogen evolution reaction in conditions of H_2 gas bubbles evolution on the RRDE, this reaction being chosen because it shall not lead to any competing reaction in the operating conditions employed (O_2-free electrolyte). This calibration was made firstly for the polycrystalline Pt disk and also for each of the Fe-Ni alloys, the Pt ring (previously cleaned by applying a few cycles of cyclic voltammetry in supporting electrolyte) being maintained at E_{ring} = 0.4 V vs RHE. The collection efficiency was close to 10% for the Pt disk, but closer to 15±2% for the different Fe-Ni alloys tested. All values are slightly below the theoretical one (owing to the harsh bubbles evolution) but correspond (for the Pt disk) or are slightly above (for the Fe-Ni disks) that found in similar conditions in [41]. It was verified that the collection efficiency remains "constant" for repeated incursion into the HER domain on the disk, which was the case if the absolute value of the disk current density remained below 10 mA cm^{-2} (*i.e.* not for very intense bubbles formation at the disk); such maximum current was targeted for any subsequent measurements, as for larger values, non-negligible noise in the measurement and depreciated collection efficiency was witnessed. Also, the potential sweep rate at the disk was set to 20 $mV.s^{-1}$, a value which is the best compromise between "stationary" measurements (that require slow sweep rate) and limited hindrance by bubbles evolution (which require as fast as possible measurement to limit bubbles accumulation). This potential sweep rate was also chosen for the OER characterizations.

3 - Then, cyclic voltamperograms of OER were plotted at each of the Fe-Ni alloy disk, while the ring was maintained at E_{ring} = 0.4 V vs RHE for O_2 detection or E_{ring} = 1.1 V vs RHE for H_2O_2 detection.

4 - The ring current was firstly baseline-corrected, then time-corrected to account for the transit-time for species to escape the disk and reach the ring, and then divided by the collection efficiency measured in HER on the given disk electrode (see point 2- above, being admitted that each electrode had its own collection efficiency).

Faradaic efficiency assessment by ICP-MS measurements. The metal ions were detected with a PerkinElmer NexION 2000c spectrometer. ^{27}Al, ^{60}Ni, ^{65}Cu, ^{93}Nb, ^{94}Mo, ^{98}Mo were analysed in standard mode. ^{48}Ti, ^{52}Cr, ^{53}Cr, ^{56}Fe, were analysed in kinetic energy discrimination (KED) mode with He, to avoid interferences with polyatomic ions. Calibration curves were determined with daily-prepared calibration solutions of Al, Ti, Cr, Fe, Ni, Cu, Nb and Mo at 0, 5, 10, 20 and 50 µg L^{-1}. ICP-MS standard solutions (Carl Roth GmbH & Co.) were diluted with 2% HNO_3 (Suprapur® 68 %, Analpure) in ultrapure water (MilliQ, 18.2 MΩ cm, TOC < 3 ppb) and 0.01 M KOH was added to have the same concentration of K in all sample solutions, to keep the same ionization of metals. The samples were diluted by 10 with 2% HNO_3. 2.5 ppb of Rh was added in all solutions to correct the instrumental drift. The percentage of recovery of internal standard was about 3% at 100%. Data were traced with the Syngistic Software. The obtained

results are summarized in Table S2, and discussed in the related section in supporting information.

Surface characterizations. The chemical composition of the different grades, after the final polishing step, was measured by scanning electron microscopy (FESEM, Field Emission Scanning Electron Microscope, ZEISS Ultra 55) coupled with elemental X-Ray energy dispersive spectrometry (EDS, BRUKER Quantax system equipped with a Silicon Drift Detector (SDD, active surface 30 mm^2), controlled with Esprit software), performed at 20 kV. In order to determine the measurement error, four 0.45 mm^2 zones per sample were analyzed.
X-ray diffraction measurements (XRD, PANalytical X'Pert Pro MPD, Cu Kα (1.5418 Å), with a Pixcel 1D detector) were realized in Bragg-Brentano configuration for the initial state characterization of all wires and plates. Grazing incidence measurements (sensitive to extreme surface), requiring larger surfaces, were performed on plates after polishing and after activations.
The surface layers created by aging and activations were characterized by transmission electron microscopy (MET JEOL 2100F - FEG - 200kV), coupled with EDS measurements (mapping mode with a 1 nm probe) and advanced imaging and diffraction tools for transmission electron microscopy (ASTAR). The TEM samples were prepared by FIB-SEM which required a protective coating (Pt was used for W-316L and carbon was used for W-825, W-718 and W-625). The active-surface-layer developed at the alloy/electrolyte interface after polishing, aging and four activations was characterized using TEM for all the samples (W-316L, W-825, W-718 and W-625 in Fig. 2a, 2b, 2c and 2d respectively). The layer thicknesses are extracted from the analysis of images with a pixel size of 0.1 nm and the statistic was performed on a length of 1.4 µm. The active-surface-layer crystallinity of the samples was further analyzed by TEM.
X-ray photoelectron spectroscopy measurements (XPS, K-Alpha apparatus from Thermo Fisher Scientific, UHV chamber (10^{-9} mbar), Al Kα radiation (1486.6eV), hemispherical analyser at 30 eV constant pass energy, constant angle of 90° between the sample surface and the analyser) were performed on the samples at initial state (after the final polishing step), after aging in the electrolyte and after activations. The position of the peaks was recalibrated with respect to the carbon peak (C 1s at 285.0 eV), the fits were performed with the background determined by the Shirley method and the fit parameters used are reported in Tables S3 to S7. More specifically, to fit the XPS data, our approach was to refer to the literature values for peak positions, their FWHM and degrees of freedom around the values (see references in Tables S3 to S7). Many iterations were performed on the 18 spectra of the Fe-Ni samples. By iteration, the position of the peaks, the FWHM and the degrees of freedom around the values were refined. No modification of peak symmetry was carried out to best match literature data. To have robust and comparable results between samples, it was chosen to optimize the fits using the same fit parameters (with few degrees of freedom) for all 18 spectra, and not to modify each fit to best match the experimental data of each sample. This constraint leads to fits that may not perfectly match the experimental values, but are the result of a global iterative optimization on a large number of spectra. This is the most relevant approach to compare "similar" materials, as is the case here. This choice was made because the absolute value of the composition of each surface was not the main target, but instead the evolution of the Fe/Ni ratio between the different samples. Allowing too much freedom to individual fits would have induced better visual match, but an error on the comparability of the results between the different spectra and samples.

References

[1] Lewis, N. S. & Nocera, D. G. Powering the planet: Chemical challenges in solar energy utilization. *Proc. Natl. Acad. Sci.* **103**, 15729–15735 (2006)

[2] Cook, T. R., et al. Solar energy supply and storage for the legacy and nonlegacy worlds. *Chem. Rev.* **110**, 6474–6502 (2010)
[3] Jiao, Y., Zheng, Y., Jaroniec, M. & Qiao, S. Z. Design of electrocatalysts for oxygen- and hydrogen-involving energy conversion reactions. *Chem. Soc. Rev.* **44**, 2060–2086, (2015)
[4] Ayers, K., et al. Perspectives on low-temperature electrolysis and potential for renewable hydrogen at scale. *Annu. Rev. Chem. Biomol. Eng.* **10**, 219–239 (2019)
[5] McCrory, C. C. L., Jung, S., Peters, J. C. & Jaramillo, T. F. Benchmarking heterogeneous electrocatalysts for the oxygen evolution reaction. *J. Am. Chem. Soc.* **135**, 16977–16987 (2013)
[6] Walter, M. G. et al. Solar Water splitting cells. *Chem. Rev.* **110**, 6446–6473 (2010)
[7] Matsumoto, Y. & Sato, E. Electrocatalytic properties of transition metal oxides for oxygen evolution reaction. *Mater. Chem. Phys.* **14**, 397–426 (1986)
[8] Gong, M. et al. An advanced Ni–Fe layered double hydroxide electrocatalyst for water oxidation. *J. Am. Chem. Soc.* **135**, 8452–8455 (2013)
[9] Louie, M. W. & Bell, A. T. An investigation of thin-film Ni–Fe oxide catalysts for the electrochemical evolution of oxygen. *J. Am. Chem. Soc.* **135**, 12329–12337 (2013)
[10] Trotochaud, L., Ranney, J. K., Williams, K. N. & Boettcher, S. W. Solution-cast metal oxide thin film electrocatalysts for oxygen evolution. *J. Am. Chem. Soc.* **134**, 17253–17261 (2012)
[11] Trotochaud, L., Young, S. L., Ranney, J. K. & Boettcher, S. W. Nickel–iron oxyhydroxide oxygen-evolution electrocatalysts: the role of intentional and incidental iron incorporation. *J. Am. Chem. Soc.***136**, 6744–6753 (2014)
[12] Corrigan, D. A. The catalysis of the oxygen evolution reaction by iron impurities in thin film nickel oxide electrodes. *J. Electrochem. Soc.***134**, 377–384 (1987)
[13] Dionigi, F. & Strasser, P. NiFe-based (oxy)hydroxide catalysts for oxygen evolution reaction in non-acidic electrolytes. *Adv. Energy Mater.* **6**, 1600621 (2016)
[14] Görlin, M. et al. Oxygen evolution reaction dynamics, faradaic charge efficiency, and the active metal redox states of Ni–Fe oxide water splitting electrocatalysts. *J. Am. Chem. Soc.* **138**, 5603–5614 (2016)
[15] Song, F. et al. Transition metal oxides as electrocatalysts for the oxygen evolution reaction in alkaline solutions: an application-inspired renaissance. *J. Am. Chem. Soc.* **140**, 7748–7759 (2018)
[16] Colli, A. N., Girault, H. H. & Battistel, A. Non-precious electrodes for practical alkaline water electrolysis. *Materials.* **12**, 1336 (2019)
[17] Brauns, J. & Turek, T. Alkaline water electrolysis powered by renewable energy: a review. *Processes*. **8**, 248 (2020)
[18] Marini, S. et al. Advanced alkaline water electrolysis. *Electrochimica Acta.* **82**, 384–391 (2012)
[19] Friebel, D. et al. Identification of highly active Fe sites in (Ni,Fe)OOH for electrocatalytic water splitting. *J. Am. Chem. Soc.* **137**, 1305–1313 (2015)
[20] Klaus, S., Cai, Y., Louie, M. W., Trotochaud, L. & Bell, A. T. Effects of Fe electrolyte impurities on $Ni(OH)_2$/NiOOH structure and oxygen evolution activity. *J. Phys. Chem. C.* **119**, 7243–7254 (2015)
[21] Enman, L. J., Burke, M. S., Batchellor, A. S. & Boettcher, S. W. Effects of intentionally incorporated metal cations on the oxygen evolution electrocatalytic activity of nickel (oxy)hydroxide in alkaline media. *ACS Catal.* **6**, 2416–2423 (2016)
[22] Mirabella, F. et al. Ni-modified Fe_3O_4(001) surface as a simple model system for understanding the oxygen evolution reaction. *Electrochimica Acta.* **389**, 138638 (2021)
[23] Wang, L. et al. Deciphering the exceptional performance of NiFe hydroxide for the oxygen evolution reaction in an anion exchange membrane electrolyzer. *ACS Appl. Energy Mater.* **5**, 2221–2230 (2022)

[24] Schäfer, H. et al. Stainless steel made to rust: a robust water-splitting catalyst with benchmark characteristics. *Energy Environ. Sci.* **8**, 2685–2697 (2015)
[25] Diaz-Morales, O., Ferrus-Suspedra, D. & Koper, M. T. M. The importance of nickel oxyhydroxide deprotonation on its activity towards electrochemical water oxidation. *Chem. Sci.* **7**, 2639–2645 (2016)
[26] Qiu, Z., Tai, C.-W., Niklasson, G. A. & Edvinsson, T. Direct observation of active catalyst surface phases and the effect of dynamic self-optimization in NiFe-layered double hydroxides for alkaline water splitting. *Energy Environ. Sci.* **12**, 572–581 (2019)
[27] Burke, M. S., Enman, L. J., Batchellor, A. S., Zou, S. & Boettcher, S. W. Oxygen evolution reaction electrocatalysis on transition metal oxides and (oxy)hydroxides: activity trends and design principles. *Chem. Mater.* **27**, 7549–7558 (2015)
[28] Spöri, C., Kwan, J. T. H., Bonakdarpour, A., Wilkinson, D. P. & Strasser, P. The stability challenges of oxygen evolving catalysts: towards a common fundamental understanding and mitigation of catalyst degradation. *Angew. Chem. Int. Ed.* **56**, 5994–6021 (2017)
[29] Maljusch, A., Conradi, O., Hoch, S., Blug, M. & Schuhmann, W. Advanced evaluation of the long-term stability of oxygen evolution electrocatalysts. *Anal. Chem.* **88**, 7597–7602 (2016)
[30] Zeradjanin, A. R. et al. Rational design of the electrode morphology for oxygen evolution – enhancing the performance for catalytic water oxidation. *RSC Adv.* **4**, 9579 (2014)
[31] Andronescu, C. et al. Powder catalyst fixation for post-electrolysis structural characterization of NiFe layered double hydroxide based oxygen evolution reaction electrocatalysts. *Angew. Chem. Int. Ed.* **56**, 11258–11262 (2017)
[32] Lafforgue, C., Maillard, F., Martin, V., Dubau, L. & Chatenet, M. Degradation of carbon-supported platinum-group-metal electrocatalysts in alkaline media studied by in situ fourier transform infrared spectroscopy and identical-location transmission electron microscopy. *ACS Catal.* **9**, 5613–5622 (2019)
[33] Möller, S. et al. Online monitoring of electrochemical carbon corrosion in alkaline electrolytes by differential electrochemical mass spectrometry. *Angew. Chem. Int. Ed.* **59**, 1585–1589 (2020)
[34] Moureaux, F., Stevens, P., Toussaint, G. & Chatenet, M. Development of an oxygen-evolution electrode from 316L stainless steel: application to the oxygen evolution reaction in aqueous lithium–air batteries. *J. Power Sources.* **229**, 123–132 (2013)
[35] Moureaux, F., Stevens, P., Toussaint, G. & Chatenet, M. Timely-activated 316L stainless steel: A low cost, durable and active electrode for oxygen evolution reaction in concentrated alkaline environments. *Appl. Catal. B Environ.* **258**, 117963 (2019)
[36] Todoroki, N. & Wadayama, T. Heterolayered Ni–Fe hydroxide/oxide nanostructures generated on a stainless-steel substrate for efficient alkaline water splitting. *ACS Appl. Mater. Interfaces.* **11**, 44161–44169 (2019)
[37] Todoroki, N., Shinomiya, A. & Wadayama, T. Nanostructures and oxygen evolution overpotentials of surface catalyst layers synthesized on various austenitic stainless steel electrodes. *Electrocatalysis.* **13**, 116–125 (2022)
[38] Kostecki R. & McLarnon, F. Electrochemical and in situ raman spectroscopic characterization of nickel hydroxide electrodes: I. Pure nickel hydroxide. *J. Electrochem. Soc.* **144**, 485–493 (1997)
[39] Lyons, M. E. & Brandon, M. P. The oxygen evolution reaction on passive oxide covered transition metal electrodes in aqueous alkaline solution. Part 1-Nickel. *Int. J. Electrochem. Sci.* **3**, 1386–1424 (2008)
[40] Li, X., Walsh, F. C. & Pletcher, D. Nickel based electrocatalysts for oxygen evolution in high current density, alkaline water electrolysers. *Phys. Chem. Chem. Phys.* **13**, 1162–1167 (2011)
[41] Chung, D. Y. et al. Dynamic stability of active sites in hydr (oxy) oxides for the oxygen evolution reaction. *Nature Energy* **5**, 222-230 (2020)

[42] Todoroki, N. & Wadayama, T. Electrochemical stability of stainless-steel-made anode for alkaline water electrolysis: Surface catalyst nanostructures and oxygen evolution overpotentials under applying potential cycle loading. *Electrochemistry Communications* **122**, 106902 (2021)
[43] Xiang, Q. et al. In situ vertical growth of Fe–Ni layered double-hydroxide arrays on Fe–Ni alloy foil: interfacial layer enhanced electrocatalyst with small overpotential for oxygen evolution reaction. *ACS Energy Lett.* **3**, 2357–2365 (2018)
[44] Dionigi, F. et al. In-situ structure and catalytic mechanism of NiFe and CoFe layered double hydroxides during oxygen evolution. *Nat. Commun.* **11**, 2522 (2020)
[45] Han, W. et al. Free-sustaining three-dimensional S235 steel-based porous electrocatalyst for highly efficient and durable oxygen evolution. *Chem. Sus. Chem.* **11**, 3661–3671 (2018)
[46] Liu, X. et al. Metal (Ni, Co)-metal oxides/graphene nanocomposites as multifunctional electrocatalysts. *Adv. Funct. Mater.* **25**, 5799–5808 (2015)
[47] Todoroki, N., Wadayama, T. Dissolution of constituent elements from various austeniticstainless steel oxygen evolution electrodes under potential cycle loadings. *International Journal of Hydrogen Energy*.**47**, 32753-32762 (2022)
[48] Neagu, D. et al. In situ observation of nanoparticle exsolution from perovskite oxides: from atomic scale mechanistic insight to nanostructure tailoring.*ACS nano*.**13**,12996-13005 (2019)
[49] Rauch, E. F. & Véron, M. Automated crystal orientation and phase mapping in TEM. *Mater. Charact.* **98**, 1–9 (2014)
[50] Dionigi, F. et al. Intrinsic electrocatalytic activity for oxygen evolution of crystalline 3D-transition metal layered double hydroxides. *Angewandte Chemie* **133** 14567-14578 (2021)
[51] Ali-Löytty, H. et al. Ambient-pressure XPS study of a Ni–Fe electrocatalyst for the oxygen evolution reaction. *J. Phys. Chem. C.* **120**, 2247–2253 (2016)
[52] Biesinger, M. C. et al. Resolving surface chemical states in XPS analysis of first row transition metals, oxides and hydroxides: Cr, Mn, Fe, Co and Ni. *Appl. Surf. Sci.* **257**, 2717–2730 (2011)
[53] McIntyre, N. S. & Zetaruk, D. G. X-ray photoelectron spectroscopic studies of iron oxides. *Anal. Chem.* **49**, 1521–1529 (1977)
[54] Asami, K. & Hashimoto, K. The X-ray photo-electron spectra of several oxides of iron and chromium. *Corros. Sci.* **17**, 559–570 (1977)
[55] Balasubramanian, M., Melendres, C. A. & Mini, S. X-ray absorption spectroscopy studies of the local atomic and electronic structure of iron incorporated into electrodeposited hydrous nickel oxide films. *J. Phys. Chem. B.* **104**, 4300–4306 (2000)
[56] Smith, R. D. L. et al. Geometric distortions in nickel (oxy)hydroxide electrocatalysts by redox inactive iron ions. *Energy Environ. Sci.* **11**, 2476–2485 (2018)
[57] Bajdich, M., García-Mota, M., Vojvodic, A., Nørskov, J. K. & Bell, A. T. Theoretical investigation of the activity of cobalt oxides for the electrochemical oxidation of water. *J. Am. Chem. Soc.* **135**, 13521–13530 (2013)
[58] Poulain, R., Klein, A. & Proost, J. Electrocatalytic properties of (100)-, (110)-, and (111)-oriented NiO thin films toward the oxygen evolution reaction. *J. Phys. Chem. C.* **122**, 22252–22263 (2018)
[59] Pourbaix, M. *Atlas of Electrochemical Equilibria in Aqueous Solutions*, National Association of Corrosion Engineers, Houston, 1979
[60] Fujita, S. et al. The effect of $Li_xNi_{2-x}O_2$/Ni with modification method on activity and durability of alkaline water electrolysis anode. *Electrocatalysis*.**9**, 162-171 (2018)
[61] Chatenet, M. et al. Electrochemical measurement of the oxygen diffusivity and solubility in concentrated alkaline media on rotating ring-disk and disk electrodes—application to industrial chlorine-soda electrolyte. *Electrochimica Acta* **45**, 2823-2827 (2000)

[62] Chatenet, M. et al. Direct rotating ring-disk measurement of the sodium borohydride diffusion coefficient in sodium hydroxide solutions. *Electrochimica Acta***54** 4426-4435 (2009)